# Segmentation-Free Quasi-Newton Method for Polyenergetic CT Reconstruction

T. Humphries and A. Faridani

***Abstract*—X-ray polychromaticity is a well-known source of artifacts in clinical CT imaging. As a polyenergetic X-ray beam passes through an object, rays with lower energy are preferentially attenuated, and thus the spectrum of the beam becomes increasingly skewed towards high-energy rays. This beam hardening phenomenon results in inconsistent projection data, and produces artifacts in images reconstructed using filtered backprojection (FBP). Methods for reducing or eliminating beam hardening artifacts can be broadly categorized into post-reconstruction approaches, which attempt to eliminate artifacts from an image reconstructed using FBP, or iterative reconstruction approaches, which attempt to reconstruct an artifact-free image from the projection data, by incorporating X-ray polychromaticity directly into the system model.**

**In this paper we compare a well-known post-reconstruction approach with an iterative approach that uses a quasi-Newton minimization algorithm. The post-reconstruction approach is a two-step process consisting of a soft-tissue correction and bone correction, while our iterative approach is based on modeling energy-dependent attenuation coefficients as a sum of photo-electric and Compton scattering components. Two numerical phantom experiments are used to demonstrate that the post-reconstruction approach does not compensate for artifacts caused by more than one different type of high attenuation material, while the iterative approach is able to reconstruct artifact-free images in both experiments. The presented iterative approach does not require any segmentation and can readily incorporate attenuation models other than the one used in this paper.**

## I. Introduction

X-ray polychromaticity is a well-known source of artifacts in clinical CT imaging. As a polyenergetic X-ray beam passes through an object, rays with lower energy are preferentially attenuated, and thus the spectrum of the beam becomes increasingly skewed towards high-energy rays. The attenuation experienced by the beam is path-dependent as a result, since the beam's spectrum is altered by the material it passes through. This *beam hardening* phenomenon results in inconsistent projection data, and produces artifacts in images reconstructed using conventional means such as filtered backprojection (FBP). These artifacts typically appear in the form of *cupping* (underestimation of attenuation coefficients, particularly towards the centre of the object), as well as dark streaking between regions of high attenuation (e.g. bone) [1].

Beam hardening (BH) artifacts reduce the qualitative and quantitative accuracy of CT images, and in some cases can impede diagnosis. Streak artifacts induced by bony structures, particularly the petrous bone in the skull [2], can be especially prominent and were identified in early scans of human patients. More recent clinical work has indicated that BH artifacts due to iodinated agents used in contrast-enhanced CT may also produce artificial perfusion defects in cardiac scans [3], [4] and "pseudoenhancement" of renal cysts [5], [6].

Department of Mathematics, Oregon State University, Corvallis, Oregon

There is no exact analytical inversion formula for data produced from polyenergetic X-rays. Thus, methods for BH correction of images produced by analytical reconstruction methods (such as FBP) are usually based on simulating monoenergetic data as a function of the acquired polyenergetic data. The simulated monoenergetic data is then used to reconstruct the image. The monoenergetic data may be generated from some empirical fitting (e.g. [7]–[9]), or by reconstructing a preliminary image and then segmenting it into different materials such as soft tissue, bone or contrast agent [10]–[12]. We refer to this class of methods as post-reconstruction approaches.

A second approach is to use iterative reconstruction methods, which attempt to reconstruct an image that is mostly free of BH artifacts directly from polychromatic data. This is achieved by including beam polychromaticity within the system model used for the reconstruction. The early 2000's saw the development of several iterative reconstruction approaches for polyenergetic data [13]–[16], and there has continued to be interest in developing these algorithms in more recent years as well [17]–[19]. Two key components of a polyenergetic iterative reconstruction method are the model used for the energy dependence of the attenuation coefficients, and the mathematical iteration used to solve the resulting nonlinear inverse problem. The model for the energy-dependent attenuation coefficients is required since it is generally not possible to independently reconstruct an attenuation map of the object for many different energies from a single set of measurements.

In this paper we develop an iterative approach which is based the attenuation model presented by De Man et al. [14], but uses a different iterative method to solve the minimization problem. The chosen iterative method is limited-memory bounded BFGS (L-BFGS-B) [20]–[22] a quasi-Newton approach. This well-known method is ideally suited to the problem because is designed for problems with high dimensionality, and allows us to impose a non-negativity constraint on the image to be reconstructed. Polyenergetic reconstruction can be implemented straightforwardly by providing an appropriate objective function and its gradient to L-BFGS-B. We present the results of numerical phantom experiments in which we compare the iterative method with a well-known post-reconstruction approach. Unlike the post-reconstruction approach, the iterative approach is able to accurately reconstruct images consisting of an arbitrary number of materials.

## II. Methodology

### A. Polyenergetic model

For polyenergetic X-ray beams, the projection measurement recorded by the $i$th detector can be modeled as

$$\mathbf{P}_i(\mu) = \int P_0(\varepsilon) \exp\left(-\mathcal{R}_i\left[\mu\left(\mathbf{x},\varepsilon\right)\right]\right)\, d\varepsilon. \tag{1}$$

Here, $\varepsilon$ represents beam energy, $P_0(\varepsilon)$ is the blank scan intensity as a function of energy (i.e. the spectrum of the beam), $\mu : \mathbb{R}^2 \times \mathbb{R} \to \mathbb{R}$ is the compactly supported, energy-dependent attenuation function corresponding to the object being imaged, $\mathbf{x}$ is position, and $\mathcal{R}_i$ represents the Radon transform of the object along the line normal to detector $i$, with $1 \leq i \leq N_{proj}$.

To reconstruct an image, we first discretize the spectrum into $N_\varepsilon$ energy levels, indexed by $h$. To approximate the integral in Eq. 1 with a sum, we choose appropriate quadrature weights $\omega_h$ for each energy level. The image itself is also discretized into $N_{pix}$ pixels, indexed by $j$. As the attenuation map of the object is energy-dependent, in principle we have $N_\varepsilon$ attenuation images of size $N_{pix}$ to reconstruct. We let $\boldsymbol{\mu}$ denote the vector consisting of all these images, and $\boldsymbol{\mu}_h$ denote only the image of size $N_{pix}$ corresponding to energy level $h$. We then have a discrete model for the projection measurements:

$$\mathbf{P}_i(\boldsymbol{\mu}) = \sum_{i=1}^{N_\varepsilon} \omega_h P_0(\varepsilon_h) \exp\left(-\mathbf{R}_i \boldsymbol{\mu}_h\right), \tag{2}$$

where $\mathbf{R}_i$ is the $i$th row of the $N_{proj} \times N_{pix}$ matrix $\mathbf{R}$ representing a discrete approximation to the Radon transform. Independently reconstructing an image corresponding to each energy level from a single set of projection measurements is a highly underdetermined reconstruction problem, which is not amenable to solution. Thus we require a model for how $\boldsymbol{\mu}$ varies with respect to energy.

### B. Iterative method

Our model for the energy dependence of $\boldsymbol{\mu}$ follows that of De Man et al. [14], where the energy dependent values $\mu(\varepsilon)$ for different materials are modeled as the sum of a photoelectric component and a Compton scattering component. The energy dependencies of the photoelectric effect $\Phi(\varepsilon)$ and Compton scattering $\Theta(\varepsilon)$ are given by known functions:

$$\Phi(\varepsilon) = \frac{1/\varepsilon^3}{1/\varepsilon_0^3}, \quad \Theta(\varepsilon) = \frac{f_{KN}(\varepsilon)}{f_{KN}(\varepsilon_0)}, \tag{3}$$

where $f_{KN}$ is the Klein-Nishina function, and $\varepsilon_0$ is some reference energy, chosen to be 70 keV in this work. We then have

$$\mu(\varepsilon) = \phi \cdot \Phi(\varepsilon) + \theta \cdot \Theta(\varepsilon), \tag{4}$$

where $\phi$ and $\theta$ are coefficients which depend on the specific material and $\varepsilon_0$. It follows from this definition that $\phi + \theta$ gives the attenuation value of the material at $\varepsilon_0$.

Reconstructing an image based on this parameterization would require estimating twice as many parameters as in a typical reconstruction problem; namely, values of $\phi$ and $\theta$ for each pixel of the image. To reduce the number of variables further, De Man et al. suggest modeling $\theta$ and $\phi$ as functions of $\mu$ at the reference energy $\varepsilon_0$, rather than as independent quantities. This is achieved by taking tabulated values [23] of $\mu(\varepsilon)$ for several materials (in this case, air, water, bone and iron) and performing a least-squares fit to obtain values of $\phi$ and $\theta$. It is then assumed that the values of $\phi$ and $\theta$ for other materials can be determined by piecewise linear interpolation. This process is illustrated in Fig. 1.

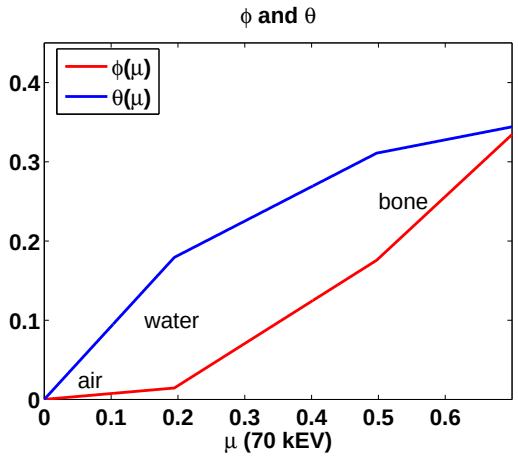


Fig. 1. Piecewise linear interpolating functions for $\phi(\mu)$ and $\theta(\mu)$. Values of $\phi$ and $\theta$ for air, water, bone and iron (not shown, $\mu$ value of 7.075 at 70 keV) are obtained from least squares fitting to the model given in Eq. 4. These are used as nodes for the piecewise linear interpolant.

Under this assumption, the problem is now simply to estimate the attenuation map of the object at the reference energy. From this point forward we refer to this map as $\boldsymbol{\mu}$. The forward model from Eq. 2 becomes:

$$\widehat{\mathbf{P}}_i(\boldsymbol{\mu}) = \sum_{h=1}^{N_\varepsilon} \omega_h P_0\left(\varepsilon_h\right) \exp\left[-\mathbf{R}_i\left(\phi(\boldsymbol{\mu}) \cdot \Phi(\varepsilon_h) + \theta(\boldsymbol{\mu}) \cdot \Theta(\varepsilon_h)\right)\right]. \tag{5}$$

While De Man et al. incorporate this model into a maximum-likelihood algorithm, we consider the reconstruction problem as one of minimizing the discrepancy between the measured data $\mathbf{P}_i$ and the forward projection of the estimate, $\widehat{\mathbf{P}}_i$ (Eq. 5), for all $i$. Since the parameters to be estimated are exponentiated, we compare the log of the projection data and minimize the function

$$G(\boldsymbol{\mu}) = \left\|\mathbf{F}(\boldsymbol{\mu})\right\|_2^2, \text{ where } \mathbf{F}_i(\boldsymbol{\mu}) = \ln \widehat{\mathbf{P}}_i(\boldsymbol{\mu}) - \ln \mathbf{P}_i. \tag{6}$$

From Equations 5 and 6 it follows that the gradient of $G$ is

$$\frac{\partial G(\boldsymbol{\mu})}{\partial \boldsymbol{\mu}_j} = 2 \sum_{i=1}^{N_{proj}} \mathbf{F}_i(\boldsymbol{\mu}) \frac{\partial \mathbf{F}_i(\boldsymbol{\mu})}{\partial \boldsymbol{\mu}_j}, \tag{7}$$

where

$$\frac{\partial \mathbf{F}_i(\boldsymbol{\mu})}{\partial \boldsymbol{\mu}_j} = \frac{-\mathbf{R}_{i,j}}{\widehat{\mathbf{P}}_i(\boldsymbol{\mu})} \sum_{h=1}^{N_\varepsilon} P_0(\varepsilon_h) \left[\Phi(\varepsilon_h) \frac{d\phi}{d\boldsymbol{\mu}_j} + \Theta(\varepsilon_h) \frac{d\theta}{d\boldsymbol{\mu}_j}\right] \times \exp\left[-\mathbf{R}_i\left(\phi(\boldsymbol{\mu}) \cdot \Phi(\varepsilon_h) + \theta(\boldsymbol{\mu}) \cdot \Theta(\varepsilon_h)\right)\right]. \tag{8}$$

We note that the objective function and its gradient can be readily vectorized. Eq. 5 can be evaluated for all $i$ simultaneously using multiplication by $\mathbf{R}$ instead of $\mathbf{R}_i$. Meanwhile,

computation of the gradient (Eq. 7) requires summing the Jacobian matrix elements (Eq. 8) over $i$. Since each Jacobian element contains a factor of $\mathbf{R}_{i,j}$, this can be implemented as a multiplication by $\mathbf{R}^T$, i.e. a backprojection operation. Thus the computation does not require access to individual elements of $\mathbf{R}$. In our experiments we implement the computation of $G$ and its gradient in Matlab, using the `radon` and `iradon` commands for forward and back projection, respectively. (The `iradon` command in Matlab is usually used for filtered back projection, but can also be called with no filter to backproject data).

To solve the minimization problem, we use limited-memory bounded BFGS (L-BFGS-B) [20]–[22], a well-known quasi-Newton method. Unlike Newton's method, quasi-Newton methods require only the gradient of the objective function to be minimized, as they construct a series of approximations to the Hessian of the function as the iteration proceeds. BFGS (Broyden-Fletcher-Goldfarb-Shanno) is the most widely used quasi-Newton method, and refers to a particular way of constructing the Hessian approximations. L-BFGS-B is a variant of BFGS in which a low-rank approximation to the Hessian matrix is used rather than a full-rank approximation. This is necessary for problems with a large number of variables (such as the one we are considering here), as a full-rank Hessian approximation is too expensive to compute and store. Furthermore, L-BFGS-B is a bounded optimization algorithm, which allows us to impose a non-negativity constraint on $\boldsymbol{\mu}$. Essentially, we are able to view L-BFGS-B as a black box, and solve the reconstruction problem by providing it with a method for computing $G$ and its gradient.

### C. Post-reconstruction correction

For the purposes of comparison, we have also implemented a well-known post-reconstruction correction approach, first presented by Joseph & Spital [10] and later by Trivedi and Herman [11]. This approach is a two-step procedure. The first step is a soft tissue correction where one simulates monoenergetic data, based on the assumption that the object consists only of soft tissue. One first determines the equivalent length of soft tissue, $T_i^s$, that the beam would pass through to generate each measurement $\mathbf{P}_i$, by solving the nonlinear equation

$$\mathbf{P}_i = \sum_{h=0}^{N_\varepsilon} \omega_h P_0(\varepsilon_h) \exp\left(-\mu_{\text{soft}}(\varepsilon_h) \cdot T_i^s\right),$$

for all $i$. One then simulates monoenergetic projection data, $\mathbf{M}_i$, at the reference energy by

$$\mathbf{M}_i = \mu_{\text{soft}}(\varepsilon_0) T_i^s,$$

and reconstructs an image from this data using FBP. This step tends to produce an image where cupping artifacts are reduced, but streaks caused by bone or other high-density materials still exist. In the second step of the method, one segments this image into regions containing bone and regions containing soft tissue. In our implementation we have used a simple thresholding approach for the segmentation. From this segmentation, one estimates the length of intersection of each ray with bone, $T_i^b$. Finally, a new estimate of $T_i^s$ is generated from solving a second set of nonlinear equations:

$$\mathbf{P}_i = \sum_{h=0}^{N_\varepsilon} P_0(\varepsilon_h) \exp\left(-\mu_{\text{soft}}(\varepsilon_h) \cdot T_i^s - \mu_{\text{bone}}(\varepsilon_h) \cdot T_i^b\right).$$

The updated monoenergetic approximation is then

$$\mathbf{M}_i = \mu_{\text{soft}}(\varepsilon_0) T_i^s + \mu_{\text{bone}}(\varepsilon_0) T_i^b,$$

which is used to reconstruct a second image with FBP.

This approach is generally successful at removing beam hardening artifacts, provided that the object does not contain tissues whose attenuation properties significantly from soft tissue and bone. It should be noted that the method can be extended to include additional materials, such as contrast agents [12]. This extension requires knowing the attenuation characteristics of every one of the constituent materials of the object, however, and may also require a more sophisticated segmentation approach to distinguish between multiple materials.

TABLE I
MATERIALS USED IN PHANTOM EXPERIMENTS ALONG WITH THEIR ATTENUATION COEFFICIENTS AT 70 KEV (IN $\text{CM}^{-1}$).

| | 1. Soft | 2. Fat | 3. Bone | 4. Dense |
|---|---|---|---|---|
| $\mu$(70 keV) | 0.1935 | 0.1717 | 0.4974 | 0.2780 |

## III. Results and conclusions

We validate the method using two $200 \times 200$ pixel numerical phantoms. The first is a circular phantom consisting of soft tissue, four small regions containing bone, and an ellipsoidal region containing fat (Fig. 3). The second phantom (Fig. 4) consists of soft tissue, three regions containing bone, and three other regions containing air, fat, and a "dense" material whose attenuation coefficient is somewhere between soft tissue and bone. Attenuation values for these materials at the reference energy are provided in Table I.

The measured projection data consist of 360 views taken over 180° and are generated by analytically computing line integrals through the geometrically-defined phantoms. This ensures that the model used to generate the data is not the same as the one used in the reconstruction. The data are averaged over 124 energies ranging from 8 to 131 keV, using a tungsten anode spectrum generated using the Siemens Spektrum online tool [24], [25]. For the purposes of reconstruction, we use only eleven energy levels, and generate the weighting coefficients $\omega_h$ using the composite trapezoid rule. The spectra used to generate the data and reconstruct the images are shown in Fig. 2.

Fig. 3 shows the results of the reconstruction for the first phantom. For the purposes of comparison, we reconstruct an image from ideal monoenergetic data using FBP (top left figure), and show a FBP reconstruction of the polyenergetic data as well, which contains typical beam hardening artifacts (top right figure). The bottom left figure contains the image obtained from the post-reconstruction correction,

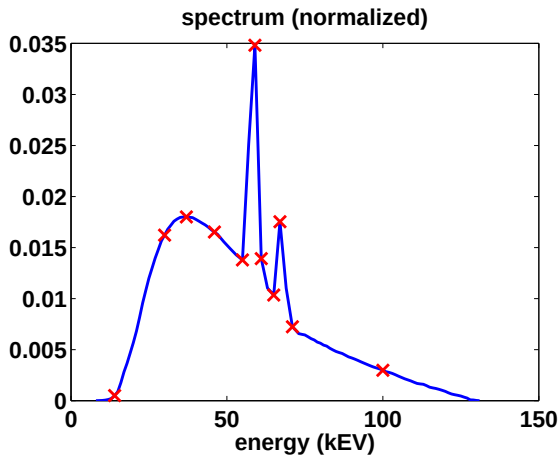


Fig. 2. Continuous and discrete spectra used to generate data and reconstruct images. Blue line shows the spectrum used to generate the data, consisting of 124 energies. Red crosses show the 11 energy levels used for reconstruction. The spectrum has been normalized so that $\int P_0(\varepsilon)\, d\varepsilon = 1$.

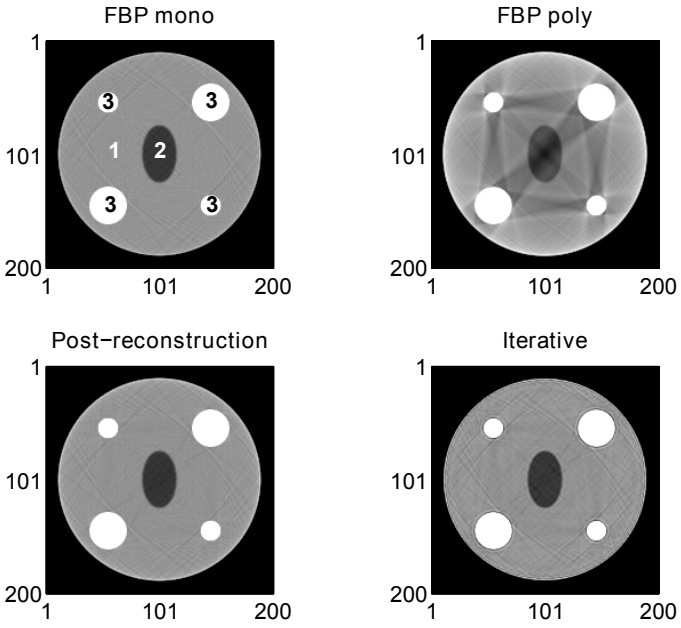


Fig. 3. Reconstructed images of first phantom. Top left: monoenergetic reconstruction, with tissue types labeled (cf. Table I). Top right: image reconstructed from polyenergetic data. Bottom left: Image reconstructed using post-reconstruction technique. Bottom right: image reconstructed using iterative technique. Greyscale window: $[0.16, 0.22]$ cm$^{-1}$.

and the bottom right figure is the image obtained from the iterative method. The image produced using the iterative method has been smoothed using anisotropic diffusion [26] to facilitate comparison with the FBP and post-reconstruction corrected images. From this figure it is apparent that both the post-reconstruction and iterative methods are effective for this phantom. Even though the post-reconstruction approach assumes the object consists only of soft tissue and bone, the attenuation characteristics of fat are sufficiently close to soft tissue for the method to be effective.

Fig. 4 shows the results of the reconstruction for the second phantom. In this instance we tried two different thresholds for the segmentation used in the post-reconstruction approach.

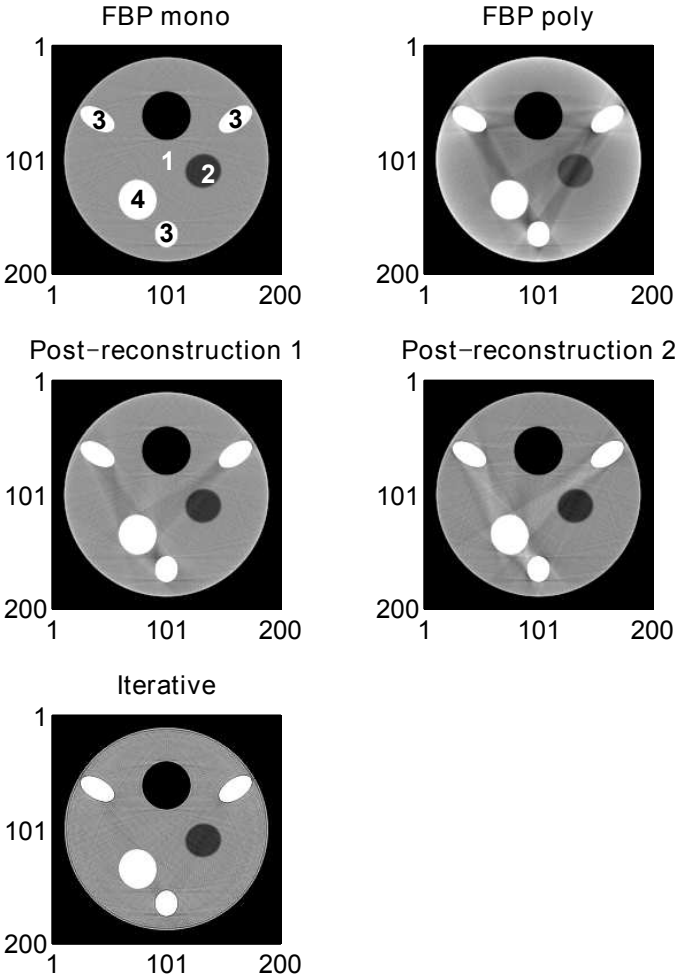


Fig. 4. Reconstructed images of second phantom. Top row again contains monoenergetic and polyenergetic FBP reconstructions. Middle row contains two reconstructions obtained using the post-reconstruction approach with different thresholds for segmentation. Bottom figure shows the result of the iterative reconstruction. Greyscale window: $[0.16, 0.22]$ cm$^{-1}$

The image labeled "Post-reconstruction 1" was obtained using a threshold where the dense region was segmented as soft tissue, while in "Post-reconstruction 2", the dense region was segmented as bone. It is clear in both cases that the presence of the dense region produces streak artifacts that the post-reconstruction correction does not remove. In fact, one can see that the streaks between any two bony regions are removed, but streaks between the dense material and a bony region are not. This is because the attenuation characteristics of the dense material differ significantly from those of bone and of soft tissue. In constrast, the iterative approach is effective in removing all of the streak artifacts.

In conclusion, we have shown that the polyenergetic reconstruction problem can be addressed using well-known nonlinear minimization methods such as L-BFGS-B, by providing an appropriate objective function and its gradient. This approach is capable of reconstructing objects containing an arbitrary number of materials and does not require any segmentation. It does require knowledge of the beam's spectrum and a model for how the attenuation of a given tissue varies as a function of energy. The algorithm is also flexible in the sense that

different attenuation models or objective functions could be used. Future work could include assessing the performance of the method in cases involving noise or other inconsistencies (e.g. imperfect knowledge of the spectrum), and reconstruction of more realistic objects.

## REFERENCES


[1] R. A. Brooks and G. Di Chiro. Beam hardening in X-ray reconstructive tomography. *Phys. Med. Biol.*, 21(3):390, 1976.

[2] M. Gado and M. Phelps. The peripheral zone of increased density in cranial computed tomography. *Radiology*, 117(1):71–74, 1975.

[3] G. A. Rodríguez-Granillo, M. A. Rosales, E. Degrossi, and A. E. Rodriguez. Signal density of left ventricular myocardial segments and impact of beam hardening artifact: implications for myocardial perfusion assessment by multidetector CT coronary angiography. *Int. J. Cardiovasc. Imag.*, 26(3):345–354, 2010.

[4] K. Kitagawa, R. T. George, A. Arbab-Zadeh, J. A.C. Lima, and A.C. Lardo. Characterization and correction of beam-hardening artifacts during dynamic volume CT assessment of myocardial perfusion. *Radiology*, 256(1):111–118, 2010.

[5] D. D. Maki, B. A. Birnbaum, D. P. Chakraborty, J. E. Jacobs, B. M. Carvalho, and G. T. Herman. Renal cyst pseudoenhancement: Beam-hardening effects on CT numbers. *Radiology*, 213(2):468–472, 1999.

[6] B. A. Birnbaum, N. Hindman, J. Lee, and J. S. Babb. Renal cyst pseudoenhancement: Influence of multidetector CT reconstruction algorithm and scanner type in phantom model. *Radiology*, 244(3):767–775, 2007.

[7] G. T. Herman. Correction for beam hardening in computed tomography. *Phys. Med. Biol.*, 24(1):81–106, 1979.

[8] M. Krumm, S. Kasperl, and M. Franz. Reducing non-linear artifacts of multi-material objects in industrial 3D computed tomography. *NDT & E International*, 41(4):242–251, 2008.

[9] Y. Kyriakou, E. Meyer, D. Prell, and M. Kachelrieß. Empirical beam hardening correction (EBHC) for CT. *Med. Phys.*, 37(10):5179–5187, 2010.

[10] P. M. Joseph and R. D. Spital. A method for correcting bone induced artifacts in computed tomography. *Journal of Computer Assisted Tomography*, 2(1):100–108, 1978.

[11] G. Herman and S. Trivedi. A comparative study of two post-reconstruction beam hardening correction methods. *IEEE Trans. Med. Imag.*, MI-2(3):128–135, 1985.

[12] P.M. Joseph and C. Ruth. A method for simultaneous correction of spectrum hardening in CT images containing both bone and iodine. *Med. Phys.*, 24(10), 1997.

[13] C. H. Yan, R. T. Whalen, G. S. Beaupré, S. Y. Yen, and S. Napel. Reconstruction algorithm for polychromatic CT imaging: application to beam hardening correction. *IEEE Trans. Med. Imag.*, 19(1), 2000.

[14] B. De Man, J. Nuyts, P. Dupont, G. Marchal, and P. Suetens. An iterative maximum-likelihood polychromatic algorithm for CT. *IEEE Trans. Med. Imag.*, 20(10):999–1008, 2001.

[15] I. A. Elbakri and J. A. Fessler. Statistical image reconstruction for polyenergetic X-ray computed tomography. *IEEE Trans. Med. Imag.*, 21(2):89–99, 2002.

[16] I. A. Elbakri and J. A. Fessler. Segmentation-free statistical image reconstruction for polyenergetic X-ray computed tomography with experimental validation. *Phys. Med. Biol.*, 48:2453–2477–99, 2003.

[17] G. Van Gompel, K. Van Slambrouck, M. Defrise, K.J. Batenburg, J. de Mey, J. Sijbers, and J. Nuyts. Iterative correction of beam hardening artifacts in CT. *Med. Phys.*, 38(7):S36–S49, 2011.

[18] Y. Lin and E. Samei. A fast poly-energetic iterative FBP algorithm. *Phys. Med. Biol.*, 59:1655–1678, 2014.

[19] Y. Lin and E. Samei. An efficient polyenergetic SART (pSART) reconstruction algorithm for quantitative myocardial CT perfusion. *Med. Phys.*, 41(2):021911–1 – 021911–14, 2014.

[20] R.H. Byrd, P. Lu, J. Nocedal, and C. Zhu. A limited memory algorithm for bound constrained optimization. *SIAM J. Sci. Comput.*, 16(5):1190–1208, 1995.

[21] C. Zhu, R. H. Byrd, P. Lu, and J. Nocedal. Algorithm 778: L-BFGS-B: Fortran subroutines for large-scale bound-constrained optimization. *ACM Transactions on Mathematical Software*, 23(4):550–560, 1997.

[22] J. Nocedal and S. J. Wright. *Numerical Optimization*. Springer, second edition, 2006.

[23] J. H. Hubbell and S. M. Seltzer. Tables of X-ray mass attenuation coefficients and mass energy-absorption coefficients. *National Institute of Standards and Technology*, 1996.

[24] Spektrum – Siemens OEM Products. https://w9.siemens.com/cms/oemproducts/home/x-raytoolbox/spektrum/pages/default.aspx.

[25] J. M. Boone and J. A. Seibert. An accurate method for computer-generating tungsten anode x-ray spectra from 30 to 140 kv. *Med. Phys.*, 24(11):1661–1670, 1997.

[26] P. Perona and J. Malik. Scale-space and edge detection using anisotropic diffusion. *IEEE Transactions on Pattern Analysis and Machine Intelligence*, 12(7):629–639, 1990.